JGR Oceans

RESEARCH ARTICLE
10.1029/2020JC016123

Submesoscale Eddy and Frontal Instabilities in the Kuroshio Interacting With a Cape South of Taiwan

Yu-Hsin Cheng[1], Ming-Huei Chang[1], Dong S. Ko[2], Sen Jan[1], Magdalena Andres[3], Anthony Kirincich[3], Yiing Jang Yang[1], and Jen-Hua Tai[4]

[1]Institute of Oceanography, National Taiwan University, Taipei, Taiwan, [2]Oceanography Division, Naval Research Laboratory, Stennis Space Center, MS, USA, [3]Department of Physical Oceanography, Woods Hole Oceanographic Institution, Woods Hole, MA, USA, [4]Research Center for Environmental Changes, Academia Sinica, Taipei, Taiwan

Key Points:
- Recirculation flow is induced, shedding submesoscale cyclonic eddies
- Headland eddy generation is influenced by the Kuroshio and tidal flows
- Eddies corotate and merge further downstream

Correspondence to:
M.-H. Chang,
minghueichang@ntu.edu.tw

Citation:
Cheng, Y.-H., Chang, M.-H., Ko, D. S., Jan, S., Andres, M., Kirincich, A., et al. (2020). Submesoscale eddy and frontal instabilities in the Kuroshio interacting with a cape south of Taiwan. *Journal of Geophysical Research: Oceans*, *124*, e2020JC016123. https://doi.org/10.1029/2020JC016123

Received 29 JAN 2020
Accepted 15 APR 2020
Accepted article online 23 APR 2020

Abstract The processes underlying the strong Kuroshio encountering a cape at the southernmost tip of Taiwan are examined with satellite-derived chlorophyll and temperature maps, a drifter trajectory, and realistic model simulations. The interaction spurs the formation of submesoscale cyclonic eddies that trap cold and high-chlorophyll water and the formation of frontal waves between the free stream and the wake flow. An observed train of eddies, which have relative vorticity about one to four times the planetary vorticity (f), is shed from the recirculation that occurs in the immediate lee of the cape as a result of flow separation. These propagate downstream at a speed of 0.5–0.6 m s^{-1}. Farther downstream, the corotation and merging of two or three adjacent eddies are common owing to the topography-induced slowdown of eddy propagation farther downstream. It is found that the relative vorticity of a corotating system ($1.2f$) is 70% weaker than that of a single eddy due to the increase of eddy diameter from ~16 to ~33 km, in agreement with Kelvin's circulation theorem. The shedding period of the submesoscale eddies is strongly modulated by either diurnal or semidiurnal tidal flows, which typically reach 0.2–0.5 m s^{-1}, whereas its intrinsic shedding period is insignificant. The frontal waves predominate in the horizontal free shear layer emitted from the cape, as well as a density front. Energetics analysis suggests that the wavy features result primarily from the growth of barotropic instability in the free shear layer, which may play a secondary process in the headland wake.

1. Introduction

The Kuroshio originates from the northern branch of the North Equatorial Current (NEC) bifurcation and is the western boundary current of the large-scale North Pacific subtropical gyre (Nitani, 1972), typically reaching flow speeds of ~1 m s^{-1} in the upper 100 m (Liang et al., 2003). After the Kuroshio's formation off the eastern coast of the Philippines, the current flows across the Luzon Strait, loops around the southern tip of Taiwan, and hugs the steep east coast of Taiwan (Figure 1a) (Liang et al., 2003). Then the Kuroshio enters East China Sea (ECS) where it flows mostly along the continental shelf break to the southeast of Kyushu Island, Japan. From the east of Luzon to the ECS, the Kuroshio's spatial and temporal variability and associated physical processes have been studied extensively (e.g., as described in Andres et al., 2011; Andres et al., 2017; Chang et al., 2018; Chang & Oey, 2011; Cheng et al., 2017; Hsin et al., 2013; Jan et al., 2017; Jan et al., 2015; Johns et al., 2001; Lee et al., 2013; Lien et al., 2014; Zhang et al., 2001). These studies focused primarily on the large-scale to mesoscale variability. Submesoscale and small-scale processes, induced primarily by topographic effects on flow along the Kuroshio from Luzon Strait to the south of Japan, are the primary interest of this study and have attracted increasing attention in recent years (Chang et al., 2019; Chang et al., 2016; Chang et al., 2013; Hasegawa et al., 2004; Liu & Chang, 2018; Nagai et al., 2017; Tsutsumi et al., 2017; Zheng et al., 2008). A variety of oceanic processes ranging from submesoscale vortices and fronts to small-scale turbulence as a result of their strong interaction has been reported. In the present context, the topographic influence of bottom drag at a sloping boundary on a strong flow, such as the Kuroshio, often converts energy from the mean flow to submesoscale vortices and to small-scale turbulent dissipation and mixing (e.g., Farmer et al., 2002; Gula et al., 2015; Molemaker et al., 2015). The turbulence could be either directly produced as the underlying mean flow interacts with topography or mediated by the instability of the submesoscale processes.

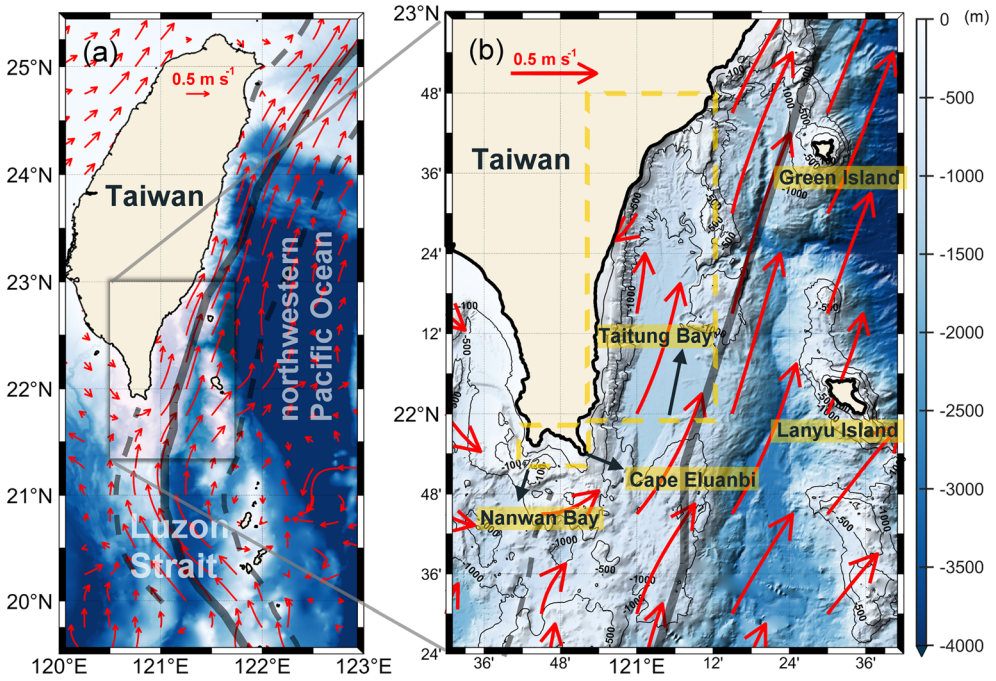

Figure 1. (a) Bathymetry (shaded color) east of Taiwan and the current field at 30 m depth (red arrows) averaged from historical shipboard ADCP data set. The black curve indicates the maximum velocity axis of Kuroshio at 15 m depth obtained from surface drifter data. The black dashed curves are the Kuroshio eastern and western boundaries defined by the 0.2 m s^{-1} isotachs at 30 m depth obtained from the average historical ADCP data (Jan et al., 2015). (b) Close-up of bathymetry and current field at 30 m depth inside the black box in Figure 1b. Black contours at the 100, 500, and 1,000 m isobaths. Yellow dashed boxes in (b) show the region of Nanwan Bay (bottom) and Taitung Bay (top).

Off southernmost Taiwan, where the Kuroshio frequently loops from the SCS back into the northwest Pacific Ocean (Figure 1a), the complex bathymetry results in energetic topographic effects on the flow. The region is characterized by abrupt topographic features, for example, headlands (Cape Eluanbi in Figure 1b), seamounts, ridges, and small islands (Green Island and Lanyu Island). Chang et al. (2013) reported that the Kuroshio-induced submesoscale wake in the lee of Green Island, a small island east of Taiwan (Figure 1b), can cause the cooler, salter, and higher chlorophyll-a concentration water to dome into the surface layer. They speculated that these water properties can be delivered downstream by eddy shedding or flow advection (Chang et al., 2013; Liu & Chang, 2018). Turbulent kinetic energy (TKE) dissipation rate on the island's leeward side is elevated, reaching levels 3 orders of magnitude larger than those typically found in the open ocean, implying the wake water properties can be diffused vertically not only via upwelling but also by turbulent mixing. Chang et al. (2019) further demonstrated that the dominant features in the wake are submesoscale vortices and shear instability in the free shear layer. The latter could enhance turbulent mixing as a result of the tilting of vertical vorticity (Farmer et al., 2002; Liu & Chang, 2018; White & Helfrich, 2013). In the wake near the island, recirculation occurs with relative vorticity 20 times that of planetary vorticity (f), and vortices are shed at a combination of periods comprising their intrinsic time scale and tidal oscillations. The latter time scale generally predominates, though the former manifests when the tidal forcing is weak. They conclude that the shedding period of the vortex is synchronized to a tidal period (Chang et al., 2019). In addition, using shipboard instruments, Chang et al. (2016) observed the effect of a seamount near Green Island on the Kuroshio. The topographic effect generates Kelvin-Helmholtz billows with a time scale of ~10 min and a vertical scale of ~100 m.

Submesoscale features, defined as having a horizontal scale of $O(10)$ km and/or Rossby number (Ro) of $O(1)$ (Capet et al., 2008; Thomas & Ferrari, 2008), normally represent the scale of ocean motions associated with transient processes. These occur over several days and serve to link the dynamics of the mesoscale with the dynamics of small-scale processes. A topic of particular interest in this context is the effect of a headland on the Kuroshio, that is, Cape Eluanbi, located at the southernmost tip of Taiwan (Figure 1b). As it exits from the Luzon Strait, the Kuroshio flows around Cape Eluanbi (Figure 1) and subsequently forms a mesoscale

recirculation (horizontal scale ~100 km by 70 km) in Taitung Bay (indicated by a yellow box in Figure 1b) as a result of flow separation (Kuehl & Sheremet, 2009; Sun et al., 2016). Though the detailed processes within this recirculation remain unclear, the effect of the sharp coastline on the Kuroshio is expected to provide a mechanism for the transition to turbulence through submesoscale processes. Understanding these transitions is important because of the practical need for parameterizations in regional-scale models of the Pacific marginal seas.

Satellite images can be used to identify regions with active submesoscale processes. Since the submesoscale features produce significant fluorescence at the sea surface—through horizontally stirring the algae and phytoplankton and by lifting layers of cooler water with nutrients into a surface mixed layer favoring the in situ phytoplankton growth (Fassbender et al., 2018; Lévy et al., 2012)—satellite remote sensing is able to capture the surface submesoscale features characterized by sea surface fluorescence and sea surface temperature (SST). Indeed, significant surface chlorophyll enhancement and cooling related to submesoscale activity is often observed in satellite images from Taitung Bay (e.g., Figure 2). Note that the magnitude and range of the signals associated with chlorophyll enhancement and cooling here are much larger than those observed in the lee of Green Island reported by Chang et al. (2013), implying an important role for these features in influencing the local Kuroshio ecosystem. By analyzing 5 years of historical CTD data in the region, Tseng et al. (2012) found enhanced turbulent mixing, estimated by the Thorpe scale method, in the lee of Lanyu Island and downstream of Cape Eluanbi. The dynamics underlying the influence of the longshore variation of the coastline geometry on the Kuroshio described above have yet to be addressed, that is, what kind of submesoscale processes there are and how are the submesoscale processes are induced.

Using the satellite imagery, drifter data, and results of numerical simulations, the characteristics of the wake where the Kuroshio flows around Cape Eluanbi are examined, together with the associated coherent submesoscale eddies and the free shear layer. The generation mechanism of the vortices and their time evolution is the central focus of this study. The satellite and drifter data and numerical model are described in section 2. The general properties, that is, the surface manifestations and vorticity and trajectory of the coherent submesoscale eddies, are described in section 3. Further evolution, generation mechanisms of the submesoscale eddies and the frontal waves within the free shear layer are examined in sections 4 and 5, respectively. Discussion and conclusions are given in section 6.

2. Data and Method

2.1. Satellite and Drifter Data

Sea surface chlorophyll-a (Chl-a) concentration and SST derived from the Moderate Resolution Imaging Spectroradiometer (MODIS) instrument are used here to characterize the submesoscale vortices southeast of Taiwan. Chlorophyll signatures in the surface are like a tracer in the sea surface, and their spatial pattern often reflects submesoscale physical processes in the ocean. Indeed, they have been widely used to study submesoscale phenomenon (e.g., Caldeira et al., 2014; Fassbender et al., 2018; Gula et al., 2015). The MODIS instrument, operated on the Terra/Aqua satellite, has a viewing swath width of 2,330 km and provides almost daily global coverage (Savtchenko et al., 2004). The sea surface variability around Taiwan is imaged twice a day during the daytime by the Terra and Aqua MODIS instruments, respectively, at around 1:00–3:00 (GMT) and 4:00–6:00 (GMT). Successive Terra and Aqua snapshots provide observations at a suitable temporal resolution to observe the submesoscale features which typically evolve over a time scale of 0.5–1 day in this region. Using the Level-2 Chl-a and SST products in swath geometry, which retain the original 1-km spatial resolution, we are able to investigate the submesoscale wake evolution, which typically has a spatial scale of $O(10)$ km. The products used here were downloaded from Ocean Color Web (https://oceancolor.gsfc.nasa.gov). Cloud mask data downloaded from NASA Earth Data Web (https://ladsweb.modaps.eosdis.nasa.gov/) were used to filter the cloud-contaminated MODIS data to improve our detection of submesoscale eddies. The geostrophic current velocities (25 × 25-km horizontal resolution) from satellite altimeters derived from the absolute dynamic topography (ADT), distributed by the Copernicus Marine Environment Monitoring Service, were used to reveal the background flows that correspond to the eddy events identified in images of satellite surface Chl-a and SST. The trajectory from a standard Surface Velocity Program (SVP) drifter (Lumpkin et al., 2017) drogued at a depth of 15 m and initially deployed in the Luzon Strait was used to validate the eddy flow field. The drifter passed southeast of Taiwan from 07

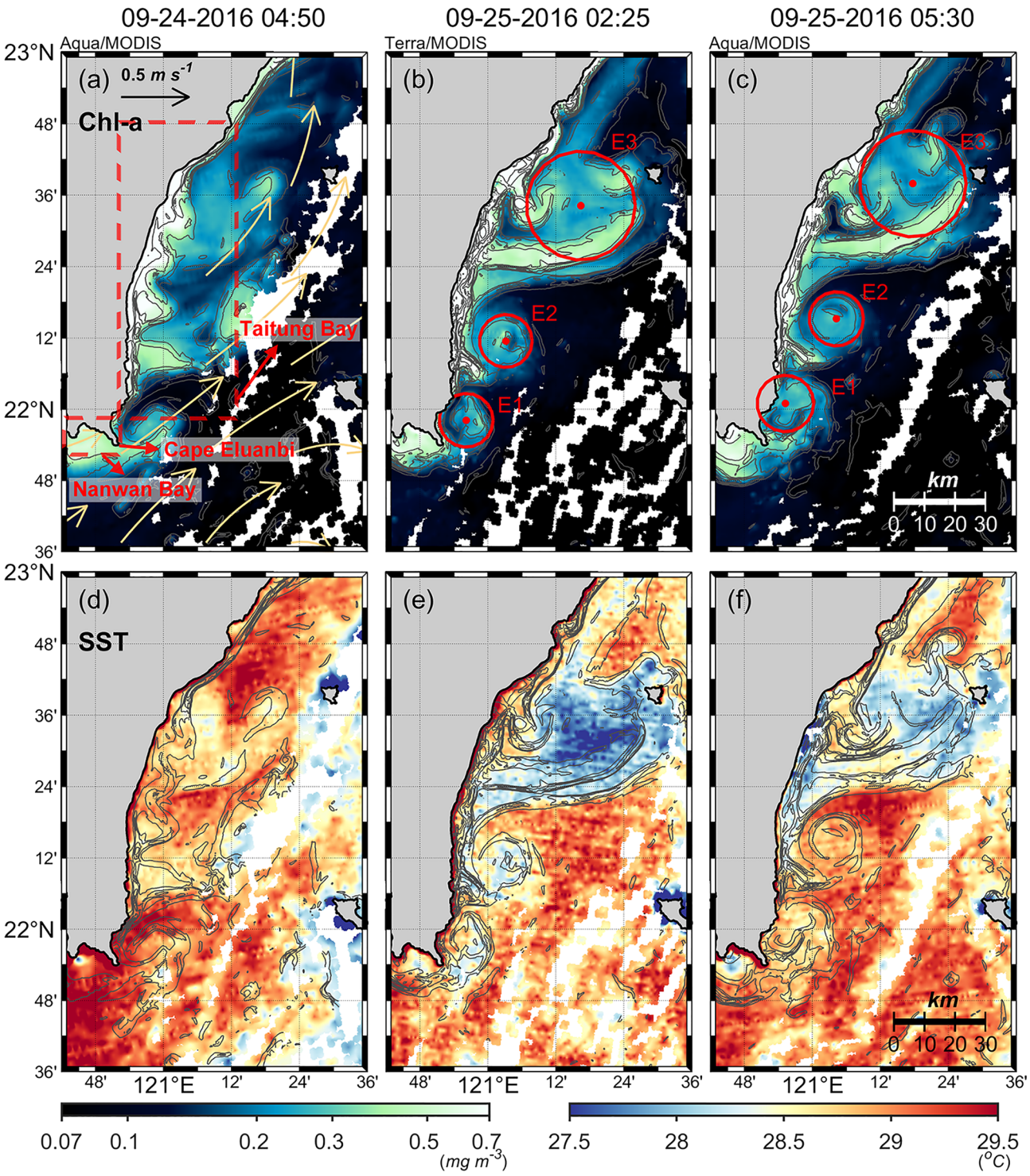

Figure 2. Sequential (top) Chl-a and (bottom) SST snapshots off southeast Taiwan. ADT-derived current velocity averaged from 22 September to 28 September is shown in yellow arrows in (a). Chl-a gradient (≥0.05 $\log_{10}$(Chla) km^{-1}) is shown in black contours at 0.05 intervals. Red circles detected by best (nonlinear) fitting the locally higher Chl-a gradients (≥0.05) encircle the eddy-like geometry, and red dots are the corresponding centers of the ideal circles. Red dashed boxes in (a) show the region of Nanwan Bay (bottom) and Taitung Bay (top).

March 2017 to 10 March 2017 (Figure 4). The sampling period of the drifter was 5 min prior to 08 March 03:00 and 1 hr thereafter. For convenience, the 5-min sampling data were subsampled to 1-hr time interval. The drifter data were downloaded from the website of Global Drifter Program (https://www.aoml.noaa.gov/phod/gdp/index.php).

2.2. Numerical Model

The high-resolution Luzon Strait Nowcast/Forecast System (LZSNFS), an application of the Ocean Nowcast/Forecast System (ONFS; Ko et al., 2009) developed by U.S. Naval Research Laboratory (NRL), is used to examine the submesoscale eddies southeast of Taiwan. LZSNFS is a realistic model, which contains the Kuroshio, mesoscale variability, and tides, and can be used to examine the formation of submesoscale eddies. The LZSNFS domain covers the region from 116°E to 125°E and from 17°N to 24°N, which includes the northern South China Sea, the Luzon Strait, and a portion of the Philippine Sea. The model horizontal resolution is ~1.3 km which is sufficient to fully resolve submesoscale eddies (~$O(10)$ km). There are 11 terrain-following σ-layers in the top 147 m and 29 z-layers below. Model topography is interpolated from 1/100° bathymetry data compiled by the Institute of Oceanography, National Taiwan University (Ocean Data Bank, http://www.odb.ntu.edu.tw/odb-webs/). The boundary conditions are derived from global HYCOM with tidal forcing from Oregon State University Tidal Prediction Software (OTPS) added at the open boundary. A high-resolution regional weather forecast model (Coupled Ocean/Atmosphere Mesoscale Prediction System, COAMPS) provides the heat and momentum flux from the atmosphere. The LZSNFS model also assimilates satellite altimeter data and Multi-Channel Sea Surface Temperature (MCSST) from satellite-derived AVHRR to improve accuracy further. LZSNFS with various configurations has been applied to a variety of studies, mainly focused on large-amplitude internal waves in the northern South China Sea (Chao et al., 2007; Chen et al., 2013; Ma et al., 2013; Qian et al., 2010; Rogers et al., 2019; Simmons et al., 2011; Warn-Varnas et al., 2015), but has also been used in other applications (Ko et al., 2009; Pickering et al., 2015; Pun et al., 2019).

3. Eddy Properties

3.1. Surface Manifestation

Submesoscale structures associated with filaments and vortices characterized by high Chl-a concentration are frequently observed in Taitung Bay. An example of three successive Chl-a and SST snapshots captured by NASA's MODIS on 24 September 04:50, 25 September 02:25, and 25 September 05:30, respectively, is shown in Figure 2. The three Chl-a and SST snapshots demonstrate the evolution of an eddy-like pattern. To help visualize the eddy features, the horizontal gradient of Chl-a, computed as $|\nabla Chla(x, y)| = \sqrt{Chla_x^2 + Chla_y^2}$, is overlaid on the surface Chl-a and SST (black curves in Figure 2). In the first snapshot (Figure 2a), a filament of high Chl-a concentration appears off Cape Eluanbi with a length scale of ~15 km. The filament slightly curves northward with a region of elevated Chl-a (0.3–0.4 mg m^{-3}) just north of the cape, forming an eddy-like structure. The second filament is found ~20 km downstream of the first filament. A larger region of high Chl-a located at the northern end of Taitung Bay can be seen further downstream. The second (Figure 2b) and third (Figure 2c) snapshots, taken 21.6 and 24.7 hr after the first, respectively, suggest that the submesoscale eddies are characterized by a "rollup" of the filament containing high Chl-a (0.3–0.7 mg m^{-3}). There is some ambiguity about whether the first and second snapshots capture the evolution of the same features since the time interval between the two is 21.6 hr which could be comparable to the time scale of the eddy evolution, as demonstrated in the next section. In contrast, the evolution from the second to the third snapshot likely captures the same features as these images are separated by only 3.1 hr. These two images suggest northward (downstream) propagation of an eddy train comprising three submesoscale eddies (denoted E1, E2, and E3 in Figures 2b and 2c). Furthermore, E1, which is in the immediate lee of Cape Eluanbi, may be in the early stage of development and still attached to the cape; this is discussed in a later section. All three images show Chl-a enrichment in Nanwan Bay off the southernmost coast of Taiwan. This is consistent with many previous studies that have shown that strong upwelling, which can lead to Chl-a enrichment, is a predominant process in Nanwan Bay (Jan & Chen, 2009; Ko et al., 2009; Lee et al., 1997). It is likely that the source of the Chl-a "dye" in the eddy train is Nanwan Bay (~0.6 mg m^{-3}). This source is implicated by the satellite-derived currents (yellow arrows in Figure 2a) that show the

Kuroshio curving back from the SCS. These currents likely advect the enriched Chl-a from Nanwan Bay to the region where the eddies are initially formed. Furthermore, the rollup of filaments associated with E1 can be clearly tracked back to Nanwan Bay as shown in Figures 2b and 2c. In principle, the offshore water in Taitung Bay, which can have high Chl-a as well (~0.7 mg m^{-3}), could be a supplementary source, especially for E2 and E3. Figure 2b shows that the concentration of Chl-a within the eddies was about 0.3–0.4 mg m^{-3} higher than their surrounding water.

The surface pattern of SST (Figures 2d–2f) associated with the eddies and filaments complements the Chl-a pattern (especially for the second snapshot) and shows that water associated with the eddy and filament and enclosed by the contours of Chl-a is 1–2 °C cooler than the ambient SST. The enrichment of Chl-a in water with lower SST may reflect an active response to submesoscale vertical exchanges which cause in situ biological responses by enhancing the nutrient supply to the sunlit zone (Lévy et al., 2012). Notably, the region of cold water in Nanwan Bay is larger in Snapshot 3 than 1, whereas the region of high Chl-a does not show significant change.

To examine the temporal and spatial evolution of the eddy train, we characterize the geometry of each eddy by fitting the locally higher Chl-a gradients ($\geq$0.05 $\log_{10}$(Chla) km^{-1}; black contours in Figure 2) to an ideal circle to estimate their areas (red circles) and the center locations (red dots). The diameters of the three eddies at 02:25 UTC (Figure 2b) are 16 km (E1), 16 km (E2), and 33 km (E3), respectively. About 3 hr later (05:30 UTC, Figure 2c), the horizontal scales are essentially the same (diameter of 17, 16, and 32 km, respectively). The horizontal scale of eddy E1 and eddy E2 is nearly identical, which is half that of E3. By tracking the eddy centers, we establish that the eddies translate northeastward 5.5, 7.2, and 7.2 km in 3.1 hr, corresponding to translation speeds of 0.50, 0.65, and 0.65 m s^{-1}, respectively, which is about half the typical Kuroshio flow speed.

A time scale associated with eddy generation may be determined from $\Delta x_{12}/V_{eddy}$, where Δx_{12}~30 km is the distance between the centers of the two adjacent eddies and V_{eddy} is the translation speed. Here we used the translation speed of E2 as V_{eddy} because E1 is likely in an early stage of development resulting in it has an ill-defined eddy structure (as discussed in section 3.2). This gives a period of ~13 hr, close to the period of the M2 tide. This strongly suggests a potential role of the tide in the eddy generation process.

3.2. Vorticity and Trajectory

To first order, the eddy-like patterns of E1, E2, and E3 have similar Chl-a snapshots at 02:25 UTC and 05:30 UTC. To account for the degree of rotation during their translations, we compute the correlation coefficient (R) between the detected eddies' Chl-a concentrations (within the red circles) at Snapshots 2 and 3 as a function of θ, the relative rotation angle of the eddies from Snapshots 2 to 3 (Figure 3). For E1, the maximum correlation of 0.53 occurs at $\theta = 69°$ (dashed line) and suggests that E1 rotates cyclonically 69° as it translates from its location in Snapshot 2 to that in Snapshot 3. The maximum correlation occurs for smaller rotation angles for the eddies translating further downstream. The maximum correlations for E2 (solid line) and E3 (dotted line) are 0.88 and 0.58, at $\theta = 60°$ and $\theta = 21°$, respectively. All three maximum correlations are statistically significant at the 95% confidence level ($R \geq 0.5$ and $P \ll 0.05$), suggesting that the three eddies detected in Snapshot 3 have indeed evolved from those in Snapshot 2 in support of our previous inference. Feature E1 has lower correlation and higher uncertainty, likely due to the ill-defined eddy structure as it is in the early stage of development in the immediate lee of the cape. Therefore, the structure at this stage, when the feature is still attached to the cape, is termed a recirculation rather than an eddy. By contrast, E2 is well developed with a higher correlation ($R = 0.88$) and low uncertainty. Further downstream, E3 shows a lower correlation, presumably due to complex eddy interactions. The horizontal scale of the eddy E3 (33 km) is about twice that of E1 and E2, indicating that there may be two eddies or more included in E3. This is investigated further with the model simulations in the next section.

The satellite images suggest that the eddies do not deform substantially during our observing period, so their rotations may resemble that of a feature in solid body rotation. Accordingly, the relative vorticity (ζ) of E2 can be simply estimated as twice the angular velocity, that is, $\zeta \approx 2(\theta/\Delta t)$, yielding a value of 1.88×10^{-4} s^{-1}, ~3.4 times of the local planetary vorticity (f). This suggests the Rossby number $Ro = \zeta/f$ of 3.4 and confirms that the dynamics fall within the regime of submesoscale process. Similarly, the Rossby numbers for E1 and E3 are 3.9 and 1.2, respectively.

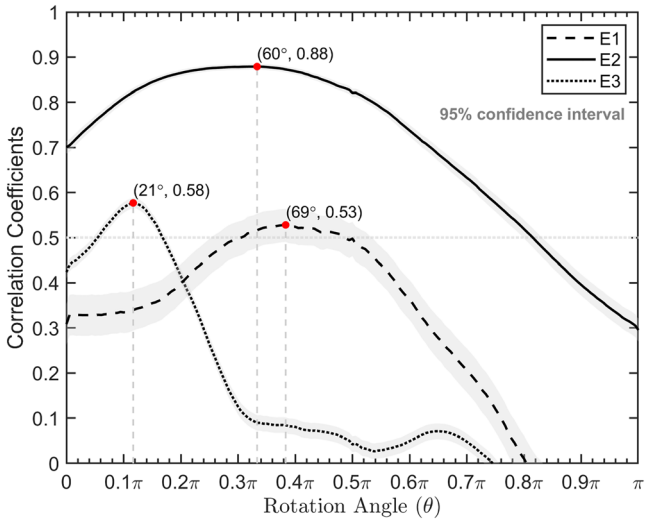

Figure 3. Correlations between the detected eddies in Snapshots 2 (Figure 2b) and 3 (Figure 2c), that is, E1 (dashed line), E2 (solid line), and E3 (dotted line). All the corresponding P values for testing the null hypothesis are less than the significance level (0.05), and the gray shaded zone denotes a 95% confidence interval for each coefficient. Each of the red dots denotes the maximum correlation with a corresponding rotation angle for the three eddy-like patterns.

The estimated properties of the submesoscale eddies discussed above are summarized in Table 1. The vorticity is similar for the cases in which the eddy scale is similar (cases E1 and E2) but is lower for the larger eddy (case E3). The larger eddy scale for E3 may be related to eddy pairing; that is, E3 may be a corotating vortex pair (Leweke et al., 2016). This is examined by using Kelvin's circulation theorem according to which the circulation (Γ) of an eddy is defined by $\Gamma = {}_D\omega dS$, where $\omega = \zeta + f$ is the absolute vorticity and dS is the surface element of D denoting the effective domain of ζ. By assuming the eddy is in solid body rotation, $\Gamma \sim \omega A$, where $A = \pi r^2$ is the area of the eddy and r is the radius of the eddy. As a result, the circulation of eddy E2 (Γ_{E2}) is $8.8f \times 10^8$ m^2 s^{-1} for $\omega = 4.4f$ s^{-1} and $A = 2 \times 10^8$ m^2 (Table 1). These E2 parameters were used as representative of both potential eddies inside E3 here. Following Leweke et al. (2016), the absolute vorticity of a corotating eddy system can be obtained by $\omega_{cr} = \frac{\Gamma_1 + \Gamma_2}{\pi b^2}$, where Γ_1 and Γ_2 are the respective circulations of two eddies and b is the distance between the centers of the two eddies. Thereby, $\omega_{cr} = 2.19f$ when $\Gamma_1 = \Gamma_2 = \Gamma_{E2}$ and $b = 16{,}000$ m—the shortest possible distance for two eddies (radius ~ 8,000 m) immediately adjacent to each other—is given, which indicates that the relative vorticity of the above system is $1.19f$ close to that of eddy E3 ($1.2f$). Our analyses suggest that eddy E3 comprises two corotating eddies in this upstream region.

A nearby drifter track from 07 March 2017 to 11 March 2017 (pink line and red dots in Figure 4) helps us confirm that these features in the Chl-a and SST maps do indeed represent a train of submesoscale eddies steered by the Kuroshio current off the southern and southeastern coast of Taiwan. On 7 March, the drifter, previously located within Nanwan Bay, was advected by Cape Eluanbi and then circulated cyclonically during its translation through the region. The second cyclonic loop occurred on 8 March followed by a much larger one in the downstream region on 9 March. The three cyclonic loops traced by the drifter's trajectory are highly analogous to the eddy train comprising E1, E2, and E3 shown in the satellite images (Figure 2), though we note that the drifter track was farther from the coast. The nearest (in time) cloudless satellite image of Chl-a was taken on 13 March 2017 (Figure 4). The snapshot shows that the patterns of elevated Chl-a concentration are roughly consistent with the circulations shown in the drifter trajectory in spite of the mismatch in timing.

While the eddy structure from the drifter and the 13 March Chl-a map is not as clear as the structures shown in Figure 2, it seems that there is an eddy in the lee of the cape with another located ~24 nautical miles offshore. This pattern resembles the alignment of eddy E1 and eddy E2 shown in Figure 2. Further downstream, an eddy-like pattern with much larger size appears near the northern end of the Taitung Bay, analogous to eddy E3 in Figure 3.

3.3. Model Interpretation

The observed eddy pattern and evolution are well simulated by LZSNFS with strong similarities between model SST (Figure 5b) and satellite SST (Figure 5a; Snapshot 2). The spatial patterns of the submesoscale eddies E1, E2, and E3 in satellite SST (Figure 5a) are well represented in the model (ME1, ME2, and ME3 in Figure 5b). Specifically, the shape and size of the model eddy ME3 are well correlated with eddy E3 observed in satellite measurements. Overall, the correlation coefficient between the satellite SST map (Figure 5a), horizontally smoothed by a spatial low-pass filter (2 km × 2 km), and the model SST (Figure 5b) is 0.6. The numerical model output includes currents which are lacking in the measurements; these modeled currents are essential in the following analysis. The model current shows primarily eastward flow south of Nanwan Bay; the flow curves northeastward after passing the cape (Figures 5b and 5c). In the numerical model output, a recirculation (denoted ME1) is formed in the immediate lee of the cape as a result of flow separation near the tip of the cape. The eddy ME2 is expected to evolve as the recirculation is shed in the lee of the cape. As previously suggested, eddy ME3 could be the result of a corotating eddy system. In the model, regions of lower temperatures associated with the submesoscale eddies are co-located with the

Table 1
Eddy Properties Estimated by Chl-a Concentration Snapshots (Figures 2b and 2c) on 25 September 2016

Symbol	Time (HH:MM)	Diameter (km)	Translating speed (m s^{-1})	Rossby number	Correlation coefficient
E1	t1 (02:25)	16	0.50	4.0	0.53
	t2 (05:30)	17			
E2	t1 (02:25)	16	0.65	3.4	0.88
	t2 (05:30)	16			
E3	t1 (02:25)	33	0.65	1.2	0.58
	t2 (05:30)	32			

regions of strong positive vorticity (Figure 5c) at $Ro \sim O(1)$, indicating ME1, ME2, and ME3 are cyclonic eddies. It is noted that the average relative vorticities of ME1, ME2, and ME3 are 4.6*f*, 3.3*f*, and 1.5*f*, respectively, slightly higher than those estimated from the satellite images. ME3 shows a significant weakening of ζ in response to the enlargement of the circulation area. The enlargement of the eddy at the northern end of Taitung Bay seems to be related to a topographic trapping effect (Figure 5c). The coastline north of the Taitung Bay curves eastward such that the northward propagating eddies are squeezed between the coastline and the Kuroshio mean flow; this leads to slowdown or arrest of the eddy. The circulation of cold water expands as a result of the interaction with the approaching eddy, and the relative vorticity weakens to conserve the potential vorticity. The interactions involve complex processes of merging and corotation of eddies, which are investigated in detail in the next section.

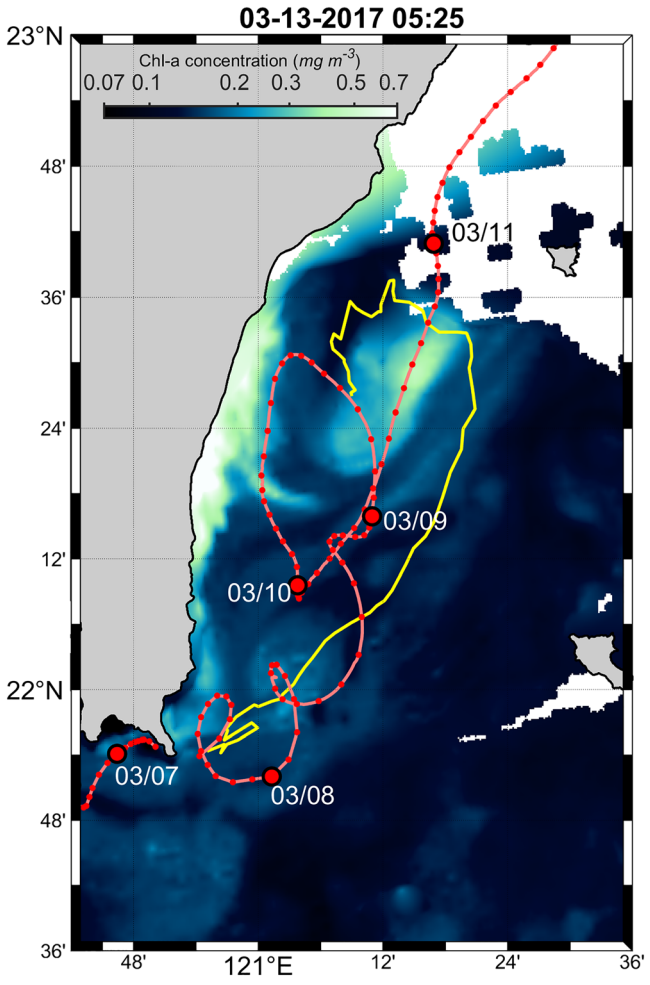

Figure 4. A composite diagram of Chl-a snapshot (shaded colors) with a drifter trajectory (pink line). Drifter positions (red dots) are shown at a 1-hr time interval. The yellow curve denotes the eddy track of CE1 shown in Figure 6, which is determined by detecting the point where ζ is maximum within the eddies.

In addition, the model shows strong vorticity within the Green Island wake (Chang et al., 2019) northeast of ME3. Notably, ME3 may have a significant impact on the flow of upstream of the Green Island wake (Figure 5c) and consequently may influence the wake flow. The submesoscale eddies may provide a link between the wake flows of Green Island to the flows downstream of Cape Eluanbi.

4. Evolution and Period

4.1. Propagation, Corotation, and Merging

As will be shown below, the presence near Cape Eluanbi of a submesoscale cold eddy is not an unusual event. The 0.6 m s^{-1} isotach, extracted from the upper 100 m of the 1-month averaged current fields, was roughly aligned with the eddy propagation path and consequently chosen to track eddies from the southern tip of Cape Eluanbi to the northern end of Taitung Bay (dashed cyan line in Figure 5c). The resulting time versus distance variations of *Ro* along the 0.6 m s^{-1} isotach (Figure 5d) show numerous northward propagating signals, characterized by a tilted band of positive *Ro*, during the 1-month model run. Those propagating signals are identified as submesoscale cyclonic eddies and indicate the nearly ubiquitous presence of these eddies during the modeled time span. The propagation speed of those eddies is 0.2–0.7 m s^{-1}, obtained by estimating the slope of the signals on the time versus distance plot.

The tracks of eddies ME1, ME2, and ME3 are determined by tracing the point where ζ is the maximum within the eddies and are overlaid on the tilted signals of phase propagation (black curves in Figure 5d). The propagating signals overlaid with the tracks of the three eddies shown in Figure 5d provide useful information to interpret their evolution. The time interval for an eddy event is ~24 hr. For ME3, the track initially remains uniform in time (i.e., flat in the time-distance diagram) as the recirculation develops. Nine hours later, the feature is shed and

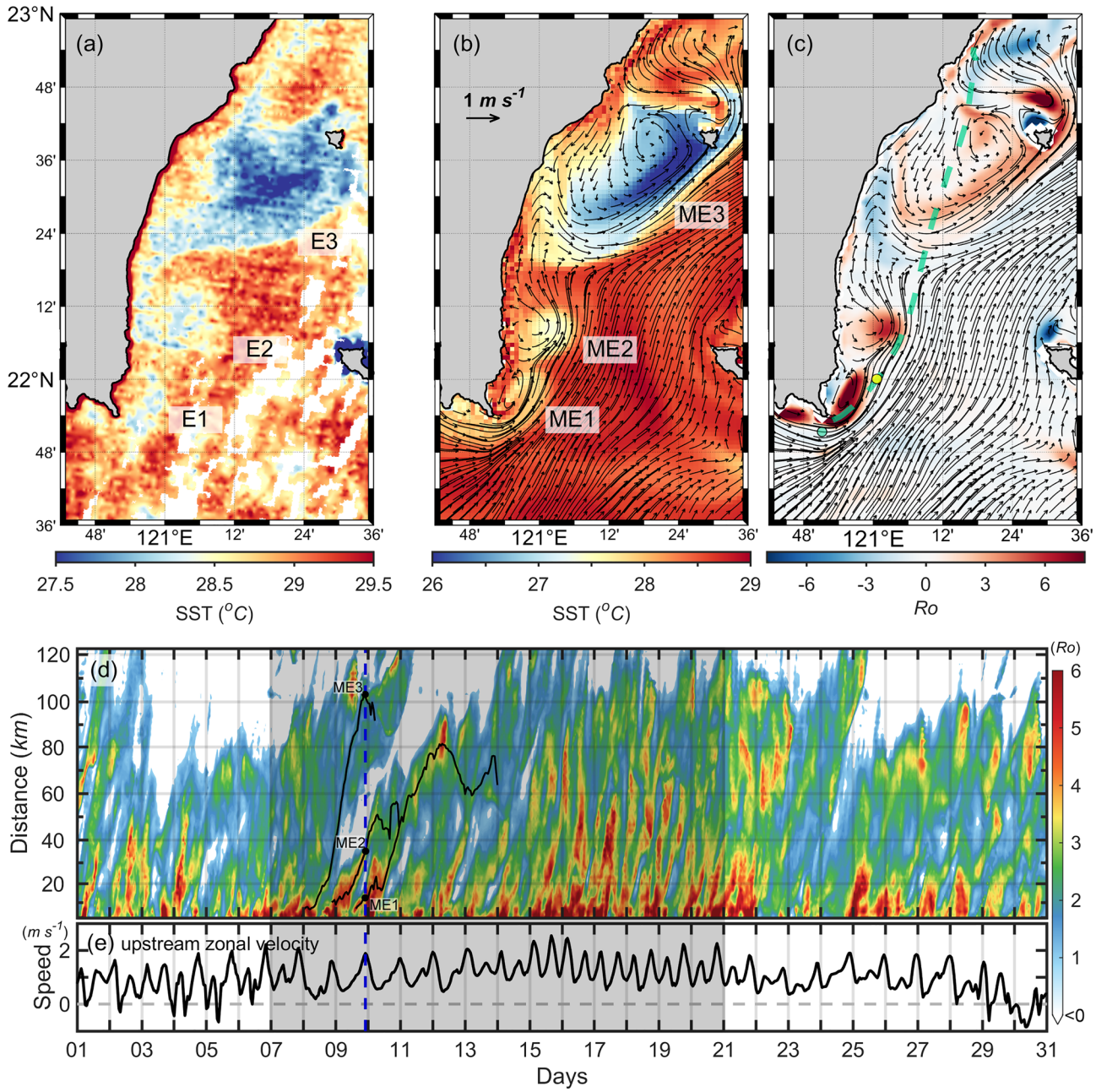

Figure 5. (a) Satellite observed SST on 25 September 2016 (as in Figure 2e). Model-derived snapshots of (b) SST and (c) relative vorticity normalized by f at 5 m depth. Black vectors denote velocity fields. The cyan dashed line in (c) shows the 0.6 m s^{-1} isotach extracted from the upper 100 m of the 1-month averaged current field. (d) A time-distance diagram of Ro (shaded color) along the 0.6 m s^{-1} isotach (cyan dashed line in (c)), revealing the propagation of eddies. Black curves denote eddy tracks of ME1, ME2, and ME3, determined by detecting the point where ζ is maximum within the eddies. Note that $Ro < 0$ is uniformly denoted by white color. (e) A time series of upstream zonal velocity (cyan dot in (c)). Blue dashed line denotes the time step of the snapshot of (c). The black shaded box denotes the region which shows detailed variations in Figure 6. The yellow dot denotes the location where SST, cross-shore speed, along-shore speed, and relative vorticity are analyzed by spectral analysis in Figure 8.

propagates downstream at an average speed of 0.5 m s^{-1}. It finally reaches 22.7°N ~2 days after its formation (i.e., see the blue dashed line in Figure 5d). Subsequently, ME3 moves slightly southward due to corotation with a preexisting eddy, and then it loses its identity. Unlike eddy ME3, the next eddy, ME2, wavers near 22.2–22.3°N for ~24 hr until ME1 catches up and merges with it to form a single eddy at Day 11 00:00 (Figure 6). The combined eddy, which is still termed ME1 here for convenience, retains its northward

propagation. Hereafter, the track of ME1 shows a latitudinal oscillation from Day 11 12:00 to Day 14 00:00. The oscillation also occurs in the following eddies, CE2 (magenta solid curve in Figure 6) and CE1 (magenta dotted curve), manifesting as a wavy curve in the time-distance diagram.

It is known that two same-signed vortices can form a corotating system, but the instability increases when the two vortices touch one another at the saddle point of the corotating system (Deem & Zabusky, 1978; Saffman & Szeto, 1980). Successive model snapshots taken at 6-hr intervals from Day 12 00:00 to Day 14 18:00 demonstrate that the latitudinal oscillation is a result of the corotation of adjacent eddies (Figure 7). On Day 12 00:00–18:00, ME1 and CE2 orbit each other while their distance decreases. On Day 13 00:00–18:00, the ME1-CE2 system corotates with the arriving CE1 and forms a complex three-eddy orbit. On Day 14 00:00–18:00, a CE2-CE1 corotating system appears due to the dispersion of ME1.

The descriptions above suggest a complex set of processes associated with eddy interactions. The drifter trajectory shown in Figure 4 lends support for the idea of eddy corotations. The track of CE1 shows a swirly line roughly along the western edge of the mean flow (magenta curve in Figure 7). The CE1 track (yellow curve) is overlaid on the drifter trajectory (pink curve) as shown in Figure 4, indicating that the track of CE1 passes through the two closed circulations related to two separate cyclonic eddies. Although the two tracks separate further north, they reveal a very similar curvature. The curvature associated with CE1 is the result of its corotation with the ME1-CE2 system as mentioned previously. Therefore, it seems reasonable that the curvature revealed by the drifter trajectory reflects the corotation as the drifter could be trapped within the corotated eddy.

4.2. Shedding Period

It is likely that the formation of submesoscale eddies results from the shedding of recirculations generated by the Kuroshio flow separation at the tip of the Cape Eluanbi. In contrast to the complex evolution dictated by the interactions of the resultant eddies, the timing of eddy formation is quite regular and corresponds to a (positive) peak value of zonal velocity in the upstream region that varies at either diurnal or semidiurnal tidal periods (Figures 5d and 5e). For example, the propagating signals that occurred on Days 8–13 and Days 24–30—when the diurnal tides were strong—show an interval of occurrence of ~24 hr. In contrast, the propagating signals that occurred on Days 15–22, when the semidiurnal tides were significant, have a shorter time interval of ~12 hr.

When the tidal periods are not dominant, it is expected that the eddy shedding period (T) should be subject to an intrinsic time scale regulated by the Strouhal number $St = L/UT$, where L is the length scale of the cape and U is the characteristic velocity (Boyer & Tao, 1987; Davies et al., 1989). To further investigate the time scale of eddy shedding, spectral analysis is applied to SST (red), cross-shore speed, along-shore speed, and relative vorticity at 22°N along the 0.6 m s^{-1} isotach (yellow dot in Figure 5c), in the immediate lee of the cape. All of these four properties reveal significant spectral peaks centered around the diurnal and semidiurnal frequencies (Figure 8). Notably, another peak with a value 1–2 orders smaller than the tidal peaks is evident with a period of 8–9 hr. In addition, we note that cross-shore speed, along-shore speed, and relative vorticity have a peak near the M4 tide; SST does not.

The intrinsic time scale suggested by St is examined next. Empirically, previous studies have found $St \sim 0.2$ in the ocean (Chang et al., 2019; Dong et al., 2007; Zeiden et al., 2019). If $St = 0.2$ is assumed for our region of interest, the resulting shedding period is ~10 hr (denoted as vertical yellow dashed line in Figure 8) by taking $L \sim 7$ km and $U \sim 1$ m s^{-1}. This value for T is close to the observed spectral peak at 8–9 hr and could indicate that this is the intrinsic shedding period in the lee of Cape Eluanbi. However, the value of $St \sim 0.2$ is based on the island wake process, although Johnston et al. (2019) report that the value also explains the shedding period in the headland wake based on the field observations near Palau. Alternatively, Davies et al. (1989) and Boyer and Tao (1987) proposed a value of $St \sim 0.09$, half of the value considered above, to study the process of a headland-generated eddy. With this value, the shedding period is ~20 hr (denoted as vertical green dashed line in Figure 8), which encompasses the peak centered at the diurnal tide.

In summary, the shedding period of submesoscale eddies is strongly modulated by the diurnal tidal flow and the semidiurnal tidal flow, as mentioned by MacKinnon et al. (2019) in the study about the generation of eddies near Palau. This is suggested both by the significant correspondence between the formation of recirculation in the lee of the cape (Figure 5d) and the peak values of the zonal tidal velocity (Figure 5e) and by

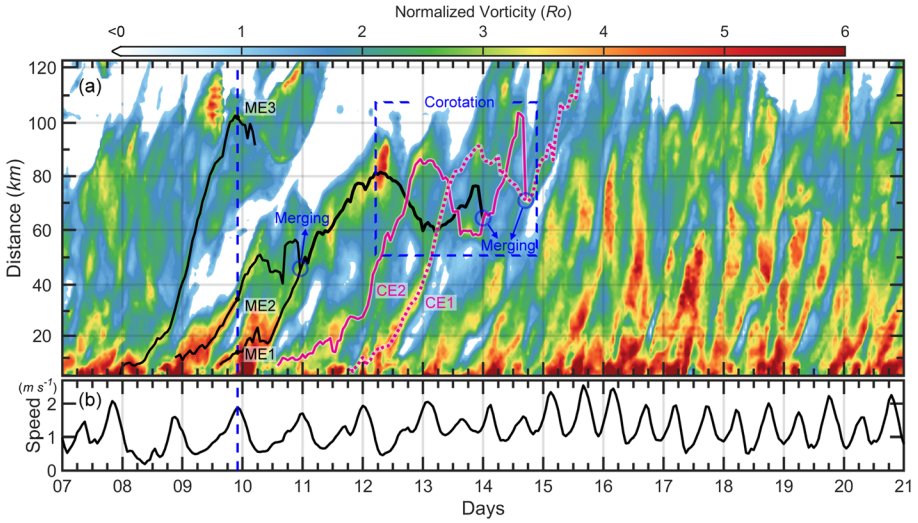

Figure 6. Detailed variations of (a) *Ro* (shaded color) along the 0.6 m s^{-1} isotach and (b) upstream zonal velocity inside the black shaded box in Figures 5d and 5e. As in Figure 5, black curves denote the eddy tracks of ME1, ME2, and ME3, and the magenta solid and dotted lines denote the eddy tracks of CE2 and CE1, respectively. The blue dashed box denotes the latitudinal oscillation due to the corotation of the adjacent eddies, and detailed evolution is shown in Figure 7.

the predominant spectral peaks centered at diurnal and semidiurnal tides (Figure 8). An intrinsic period of submesoscale eddy formation, based on *St*, may also play a role in our region of interest. Depending on the assumed *St*, this period may be ~20 or ~10 hr. However, we note that the former period falls within the tidal signal and the latter period has a relatively weak signal in the numerical model output. Hence, it is difficult to ascertain definitively what *St* is in our region of interest.

5. The Wavy Front

In addition to the primary processes (the recirculation and eddy shedding in the lee of Cape Eluanbi as described in the previous section), the front between the free stream (mean flow) and the wake flow in Taitung Bay frequently exhibits a wavy feature, which can act as a secondary process active within the headland wake (Figure 7). This wavy front separates the warm mean flow on its eastern side from the cool but highly variable watermasses on its western side as shown in Figure 7. Although the wavy feature results partly from vorticity deformation and stretching, the wavy front is a predominant feature when the upstream flow is more northward and approaches the coast resulting in a narrower/fragmented recirculation (Figure 9). Therefore, although we expect the recirculation and the eddy shedding to be a dominant process, it is not the only important submesoscale process in Taitung Bay.

Two examples on Model Day 17 (Figure 9b) and Day 18 (Figure 9e) show significant wavy fronts trapping the cold water in Taitung Bay, with their corresponding (similar) satellite SST shown in Figures 9a and 9d, respectively. The wavy feature is characterized by the rollup thermal pattern as shown in Figure 9a. The length scale of the frontal wave suggests that these can be categorized as submesoscale features (i.e., tens of kilometers). As indicated by the current vectors, the structure of the recirculation (or eddy) is ambiguous. This can be further demonstrated by the vorticity (Figures 9c and 9f). Well-defined eddy vorticity patterns, as shown in Figure 7, are absent here. Instead, a band of strong vorticity, representing the free shear layer emitted from the southern tip of the cape, is co-located with the wavy front. This suggests that the formation of the wavy front is related to the strong lateral shear.

The combination of a strong horizontal shear layer and a density front points to the likely formation of the wavy features as a result of barotropic or/and baroclinic instability. Both types grow at the expense of the total mean flow energy. The barotropic instabilities grow by extracting kinetic energy via the shear flow (e.g., Gula et al., 2015), whereas the baroclinic instabilities result from the release of potential energy due to the gravitational collapse at a density front (e.g., Boccaletti et al., 2007). We perform an energetics

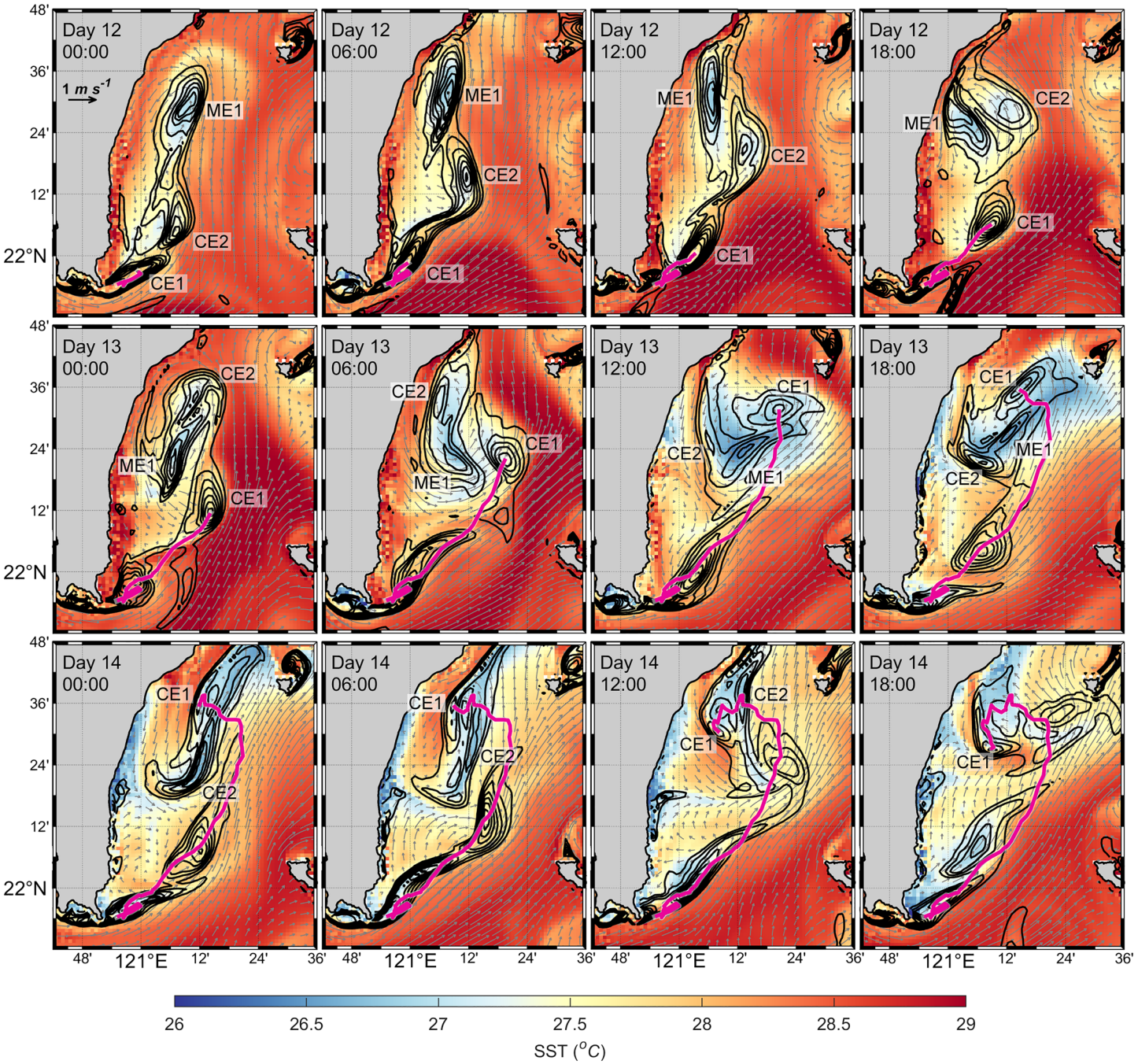

Figure 7. Model snapshots of sea temperature at 5 m depth (shaded color) taken at a time interval of 6 hr from Day 12 00:00 to Day 14 18:00. Black curves denote ζf^{-1} from 1 to 8 with an interval of 1. Vectors denote velocity fields. The magenta curve denotes the eddy track of CE1.

analysis on the eddy-mean flow interactions (Dong et al., 2007; Gula et al., 2014; Kang & Curchitser, 2015) based on our 1-month LZSNFS numerical model output to identify the relative importance of these two processes. In our analysis, the x and y components represent the zonal (east-west) and meridional (north-south) components, respectively. Velocities are expressed as u, v, and w for zonal, meridional, and vertical components, respectively, and the density is ρ. The flow is decomposed into the mean field and perturbations, respectively denoted as an overbar and a prime, that is, $u = \overline{u} + u'$, $v = \overline{v} + v'$, $w = \overline{w} + w'$, and $\rho = \overline{\rho} + \rho'$. The overbar represents the value of the time mean over our 1-month model output. The

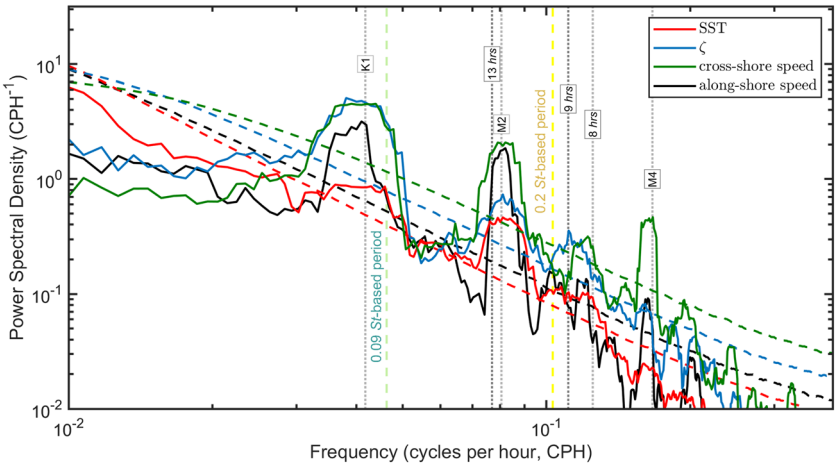

Figure 8. Spectra of SST (red curve), surface relative vorticity (blue curve), cross-shore speed (green curve), and along-shore speed (black curve) at 22°N on 0.6 m s^{-1} isotach (yellow dot in Figure 5c). Four variables were normalized by the standard deviation of themselves while doing power spectral analysis. The dashed curve is the 95% confidence level spectrum based on a χ^2 test performed on the mean spectrum of the red noise (Oppenheim, 2010). The vertical gray dotted lines denote spectral peaks at 23.92 hr (K1), 12.42 hr (M2), 9 hr, 8 hr, and 6.21 hr (M4). In addition, the gray dotted line at 13 hr denotes the time scale of the eddy generation determined by the snapshots in Figures 2b and 2c. The vertical green and yellow dashed line denotes the *St*-based periods with *St* ~ 0.09 and ~0.2, respectively.

perturbations represent the processes associated with instabilities. Following Gula et al. (2014) and Dong et al. (2007), the conversions from mean flow kinetic energy to associated perturbation kinetic energy due to the horizontal shear and vertical shear are expressed as HRS and VRS, respectively, where

$$HRS = -\rho_0\left(\overline{u'^2}\frac{\partial u^-}{\partial x} + \overline{u'v'}\frac{\partial \overline{u}}{\partial y} + \overline{v'^2}\frac{\partial \overline{v}}{\partial x} + \overline{u'v'}\frac{\partial \overline{v}}{\partial y}\right), \quad (1)$$

obtained from the product of horizontal mean shear and Reynolds stress, and

$$VRS = -\rho_0\left(\overline{u'w'}\frac{\partial \overline{u}}{\partial z} + \overline{v'w'}\frac{\partial \overline{v}}{\partial z}\right), \quad (2)$$

the product of vertical shear of the mean flow and vertical Reynolds stress. The value of ρ_0 is 1,024.8 kg m^{-3}. The conversion of eddy potential energy to eddy kinetic energy is

$$\mathrm{VBF} = -g\overline{w'\rho'}. \quad (3)$$

The magnitude of positive HRS + VRS and VBF, respectively, measure the importance of the generation of perturbation kinetic energy by the barotropic instability versus that by baroclinic instability. Figure 10a shows a significant band of positive depth-integrated HRS (denoted as yellow box b), roughly along the 0.6 m s^{-1} isotach (black dashed line), where the strong horizontal shear layer and density front is present. The strongest value of area-integrated HRS ~10 kJ m^{-1} s^{-1} appears in the immediate lee of Cape Eluanbi (red curve in Figure 10d) and weakens downstream. The negative depth-integrated HRS appears north of Taitung Bay (denoted as yellow box a), implying that the eddy kinetic energy is hardly generated and may even be converted back to mean flow kinetic energy here (Gula et al., 2015). The conversion of eddy kinetic energy to mean flow kinetic energy may be related to eddy attenuation and the complex eddy interactions described previously. In addition, the active conversion region where the depth-integrated HRS > 0 also includes water near Lanyu Island and Green Island and on the ridge in the Luzon Strait. It is noted that the HRS near Green Island (3–4 J m^{-2} s^{-1}, as Liu & Chang, 2018, suggested) is ~3 times larger than that near Cape Eluanbi (~1 J m^{-2} s^{-1}).

Figure 10b shows the spatial distribution of depth-integrated VRS as a proxy for energy conversion via vertical shear. Unlike the depth-integrated HRS, this indicates a region of negative values (denoted with the

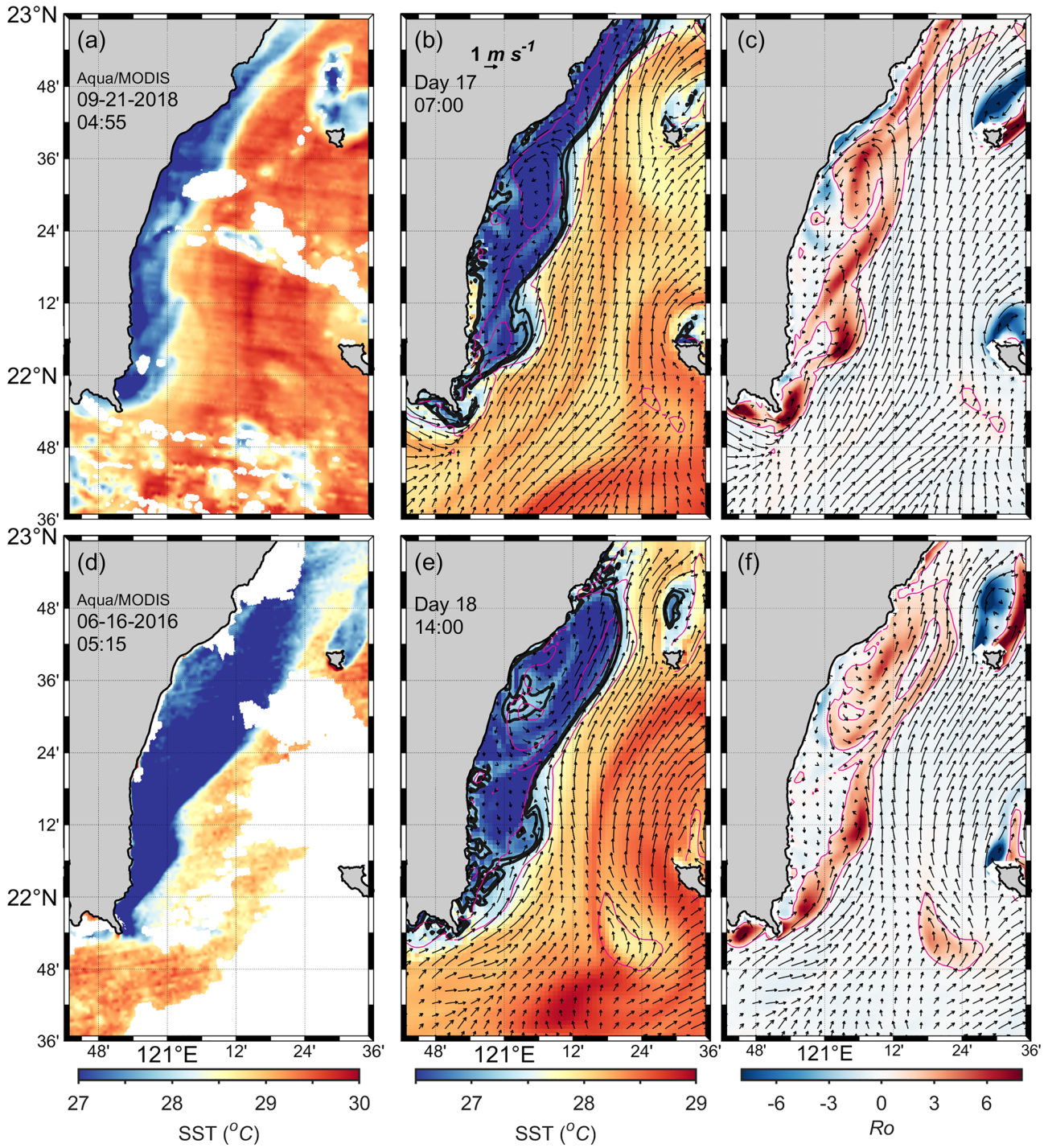

Figure 9. (a) Satellite-observed SST on 21 September 2018. Model snapshots of (b) SST and (c) ζf^{-1} at 5 m depth on Model Day 17. As in (a)–(c), but on (d) 16 June 2016 and on (e) and (f) Model Day 18. Vectors denote velocity fields. The black curves in (b) and (e) denote the 27 and 27.2 °C isotherm. The magenta curves denote $\zeta f^{-1} = 1$.

yellow box in Figure 10b) that is primarily located on the eastern side of wavy front (0.6 m s^{-1} isotach). The processes that can induce the energy feedback to the background mean flow are unknown. The depth-integrated VBF is generally weak except for that above the ridges in the Luzon Strait which have no correspondence with the wavy front.

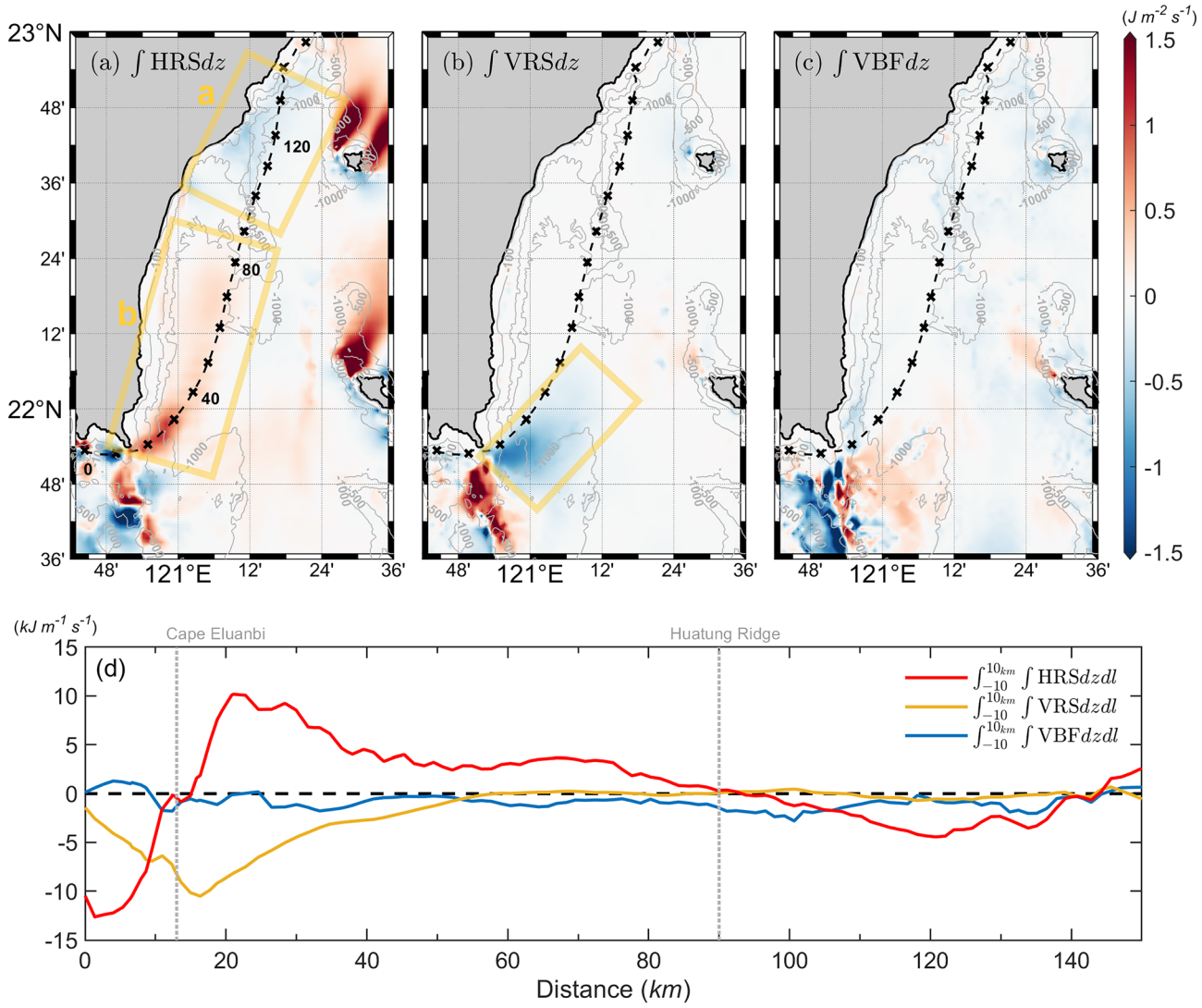

Figure 10. Monthly mean barotropic conversion terms (a) $\int$HRSdz and (b) $\int$VRSdz field and baroclinic conversion term (c) $\int$VBFdz field. These quantities are integrated vertically over the entire water column from surface to bottom. Topography is shown in gray contours at the 100, 500, and 1,000 m isobaths. The dashed line shows the 0.6 m s^{-1} isotach with markers at a 10-km interval. (d) Variations of $\int_{-10}^{10\ km}\int$HRS$dzdl$ (red), $\int_{-10}^{10\ km}\int$VRS$dzdl$ (yellow), and $\int_{-10}^{10\ km}\int$VBF$dzdl$ (blue) along the 0.6 m s^{-1} isotach. The l components represent the cross-transect components.

In summary, along the 0.6 m s^{-1} isotach, the area-integrated HRS (red curve in Figure 10d) is predominant and remains positive from 12 to 90 km, indicating energy conversion from the mean flow to the perturbations. Therefore, it is expected that the wavy features result primarily from barotropic instability that grows in the strong free shear layer generated in the lateral boundary of Cape Eluanbi.

6. Discussion and Conclusions

As the Kuroshio flows around Cape Eluanbi (length scale ~7 km), the effect of the sharp coast on the current gives rise to flow separation near the tip of the cape. This topographic effect precipitates a recirculation in the immediate lee of the cape and a strong free shear layer between the free stream and the wake flow. Here we explore in detail for the first time the dynamics underlying the effect of the longshore variations of coastline geometry southeast of Taiwan on the Kuroshio. In the present study, the generation of the wake, coherent submesoscale eddies, and the free shear layer in the lee of Cape Eluanbi are examined by the satellite imagery, drifter data, and realistic numerical model simulations. The combination of Chl-a

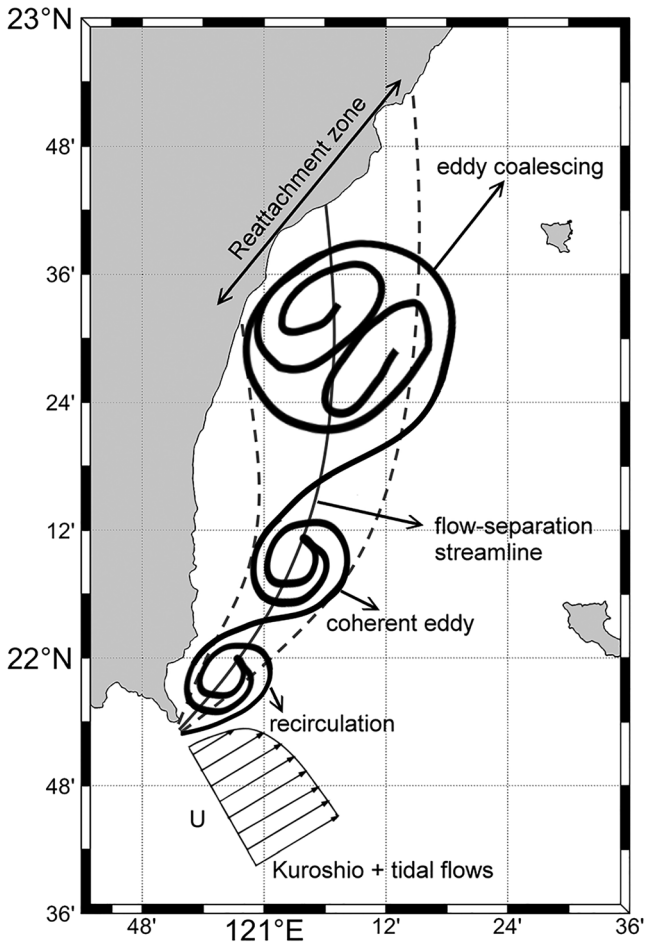

Figure 11. A schematic diagram of eddy evolution in the lee of Cape Eluanbi.

and SST snapshots captured by satellite images and drifter trajectories highlights submesoscale eddies that are frequently observed in Taitung Bay. Three successive Chl-a and SST snapshots from 24 September 04:50, 25 September 02:25, and 25 September 05:30 demonstrate the evolution of the submesoscale eddies. These clearly show the downstream propagation (0.5–0.6 m s^{-1}) of an eddy train composing three submesoscale eddies, that is, E1 (diameter ~ 16 km, ζ~3.9f), E2 (~16 km, ζ~3.4f), and E3 (~33 km, ζ~1.2f). The relative rotation angle is estimated by computing the maximum correlation coefficient between the detected eddies at 02:25 and 05:30. Accordingly, the relative vorticities can be simply estimated based on the spin of a solid body. Eddy E3, whose horizontal scale is about twice of that of E1 and E2, could be a result of corotating eddies in the upstream, which is supported by the absolute vorticity estimation of a corotating eddy system (Leweke et al., 2016) and by our numerical model interpretation. The surface pattern of SST associated with the eddies and filaments (i.e., in which temperature is 1–2 °C cooler than the ambient SST) agrees with the pattern of Chl-a. The enriched Chl-a within E1 is likely advected from Nanwan Bay via the Kuroshio's curving path. Besides, the enriched Chl-a observed within E2 and E3 could be advected from the Taitung Bay and/or enhanced by in situ biological responses related to upwelling nutrients.

The observed eddy patterns and evolution are well simulated by the realistic model, LZSNFS, essentially filling the lack of current velocity in the analysis based on satellite images. The time versus latitude variations of positive *Ro* (representative of cyclonic eddies) along the 0.6 m s^{-1} isotach show numerous northward propagating signals (0.2–0.7 m s^{-1}) in the region during the 1-month model duration. The tracks of eddies, established by the maximum ζ within the eddy, reveal latitudinal oscillations that manifest as twisting tracks in the time-distance diagram. These are a result of the corotation of the adjacent eddies. In summary, the observations and model results suggest that submesoscale cyclonic eddies are formed by the shedding of a recirculation feature generated by Kuroshio flow separation at the tip of Cape Eluanbi. Next, the eddy propagates downstream and catches up to a preexisting eddy. After that, the cyclonic eddies form a corotating system and merge to form a single eddy near 22.7°N. These complex processes associated with the eddy interactions are summarized in a cartoon that depicts the scenario we suggest (Figure 11).

The wavy feature in the bay results not only from vorticity deformation/stretching but also from shear instability, which may act as another important process in the headland wake region. The wavy feature generated along the lateral boundary of Cape Eluanbi is related to the combination of a strong horizontal shear layer and a density front. Results of the energetics analysis employed to explore the eddy-mean flow interactions demonstrate that the HRS is predominant in the southern Taitung Bay, indicating that the energy transfer is primarily through barotropic instability. Along the 0.6 m s^{-1} isotach, the strongest value of the area-integrated HRS (~10 kJ m^{-1} s^{-1}) appears in the immediate lee of the cape and remains positive in the region south of Taitung Bay. In contrast, the negative depth-integrated HRS appears in the north of Taitung Bay, implying the eddy kinetic energy is hardly generated and may be converted back to mean flow kinetic energy due to eddy attenuation and complex eddy interactions. Although barotropic instability can also grow into submesoscale eddies that appear like a vortex train on satellite snapshots, the physical mechanism is different from the shedding of a recirculation feature. The former can grow anywhere during the presence of a free shear layer (Smyth & Carpenter, 2019). The latter arise from flow separation caused by an abrupt change of topography, providing a form drag on the incident flow, and can be shed downstream as Reynolds number increases (Williamson, 1996). However, we did not find the eddies involved from the frontal waves (barotropic instability) from our present numerical model and satellite images.

The shedding period of submesoscale eddies is strongly modulated by diurnal or semidiurnal tidal flow. This is supported by two lines of evidence. First, the timing of eddy formations is regular and corresponds to a local maximum value of eastward velocity in the upstream region associated with diurnal or semidiurnal tidal periods. Second, spectral analysis of SST, relative vorticity, and cross-shore and along-shore speeds reveals spectral peaks centered around the diurnal, semidiurnal, and 8–9 hr periods. The (non-tidal) intrinsic shedding period regulated by the *St* is estimated here as ~10 or ~20 hr, respectively, assuming *St* ~ 0.2 (for an island-generated eddy, Johnston et al., 2019) or *St* ~ 0.09 (for a headland-generated eddy, Davies et al., 1989), and may play a role in setting the intrinsic time scale (though we note that the tidal time scales seem to dominate here). However, the process of the headland-generated eddy is slightly different from that of an island-generated eddy. For example, an island wake often results in alternate shedding of positive and negative vortices forming a vortex street. In contrast, a headland wake only generates either all positive or all negative vortices. Besides, the behavior of eddy generation for a combination of mean and oscillatory flow is different with for either alone, depending on the ratio of speeds (MacKinnon et al., 2019). Southeast of Taiwan, the Kuroshio's speed ~1 m s^{-1} in the upper 100 m (Liang et al., 2003) is larger than the speed variation of tidal flow (~ $\pm$ 0.3 m s^{-1}, Jan & Chen, 2009). Our results show that the eddies all have the same sign of vorticity (cyclonic) in the Taitung Bay, agreed with the study's results in Palua (MacKinnon et al., 2019).

By interpreting our satellite observations with the output from a realistic numerical model simulation, we infer that the effect of Cape Eluanbi on the Kuroshio can result in (1) a recirculation in the lee of the cape, further shedding downstream as a train of submesoscale cyclonic eddies, and (2) forms a strong vorticity filament inducing horizontal shear instabilities when the upstream flow is more northward and approaches the coastline resulting in a narrower/fragmented recirculation. Chl-a concentration, increasing about three to four times by these processes, plays a key role in the localized circulation of chemical elements by an ecosystem. In the Kuroshio regime from Luzon to Japan, many abrupt topographic features may affect the flow, such as described in the present study. The Kuroshio carries a large amount of heat and momentum poleward and has a potential impact on biogeochemical processes along its path through nutrient transport (Liu et al., 2014). Submesoscale eddies may provide horizontal and vertical aspects to nutrient transport within the Kuroshio. As mentioned in the introduction, understanding these transitions is important due to the practical need for parameterizations in regional-scale models of the Pacific marginal seas. This study has given a specific description of the features of these processes in the Taitung Bay, one of abrupt topography on the Kuroshio path.

Acknowledgments
Discussions with Dr. Thomas Peacock, Dr. Ren-Chieh Lien, and Dr. Guan-Yu Chen significantly improved our physical analysis. The Ssalto/Duacs altimeter products were produced and distributed by the Copernicus Marine and Environment Monitoring Service (CMEMS) (http://www.marine.copernicus.eu). NASA Goddard Space Flight Center, Ocean Ecology Laboratory, Ocean Biology Processing Group. Moderate-resolution Imaging Spectroradiometer (MODIS) Aqua Ocean Color Data; 2018 Reprocessing. NASA OB.DAAC, Greenbelt, MD, USA. doi: 10.5067/AQUA/MODIS/L2/OC/ 2018. Pawlowicz, R., 2019. "M_Map: A mapping package for MATLAB," version 1.4k, [Computer software], available online (at www.eoas.ubc.ca/~rich/map.html). We thank the MOST Ocean Data Bank for providing bathymetry data (http://www.odb.ntu.edu.tw/odben/). Yu-Hsin Cheng was supported by the CWB of Taiwan through Grant 1062076C. Ming-Huei Chang was supported by the Ministry of Science and Technology of Taiwan (MOST) under Grants 103-2611-M-002-018, 105-2611-M-002-012, and 107-2611-M-002-015. Sen Jan was supported with MOST Grants 101-2611-M-002-018-MY3, 103-2611-M-002-011, and 105-2119-M-002-042. Magdalena Andres was supported by the U.S. Office of Naval Research Grant N000141613069. Data used to produce the figures and analyses in this article can be obtained online (from https://doi.org/10.5281/zenodo.3621259).

References

Andres, M., Kwon, Y.-O., & Yang, J. (2011). Observations of the Kuroshio's barotropic and baroclinic responses to basin-wide wind forcing. *Journal of Geophysical Research*, *116*, C04011. https://doi.org/10.1029/2010JC006863

Andres, M., Mensah, V., Jan, S., Chang, M.-H., Yang, Y.-J., Lee, C. M., et al. (2017). Downstream evolution of the Kuroshio's time-varying transport and velocity structure. *Journal of Geophysical Research: Oceans*, *122*, 3519–3542. https://doi.org/10.1002/2016JC012519

Boccaletti, G., Ferrari, R., & Fox-Kemper, B. (2007). Mixed layer instabilities and restratification. *Journal of Physical Oceanography*, *37*(9), 2228–2250. https://doi.org/10.1175/jpo3101.1

Boyer, D. L., & Tao, L. (1987). On the motion of linearly stratified rotating fluids past capes. *Journal of Fluid Mechanics*, *180*, 429–449. https://doi.org/10.1017/S0022112087001885

Caldeira, R. M. A., Stegner, A., Couvelard, X., Araújo, I. B., Testor, P., & Lorenzo, A. (2014). Evolution of an oceanic anticyclone in the lee of Madeira Island: In situ and remote sensing survey. *Journal of Geophysical Research: Oceans*, *119*, 1195–1216. https://doi.org/10.1002/2013JC009493

Capet, X., McWilliams, J. C., Molemaker, M. J., & Shchepetkin, A. F. (2008). Mesoscale to submesoscale transition in the California Current System. Part I: Flow structure, eddy flux, and observational tests. *Journal of Physical Oceanography*, *38*(1), 29–43. https://doi.org/10.1175/2007jpo3671.1

Chang, M.-H., Jan, S., Liu, C.-L., Cheng, Y.-H., and Mensah, V. (2019). Observations of island wakes at high Rossby numbers: Evolution of submesoscale vortices and free shear layers, *Journal of Physical Oceanography*, *49*(11), 2997–3016. https://doi.org/10.1175/jpo-d-19-0035.1

Chang, M.-H., Jan, S., Mensah, V., Andres, M., Rainville, L., Yang, Y. J., & Cheng, Y.-H. (2018). Zonal migration and transport variations of the Kuroshio east of Taiwan induced by eddy impingements. *Deep-Sea Research Part I*, *131*, 1–15. https://doi.org/10.1016/j.dsr.2017.11.006

Chang, M.-H., Jheng, S.-Y., & Lien, R.-C. (2016). Trains of large Kelvin-Helmholtz billows observed in the Kuroshio above a seamount. *Geophysical Research Letters*, *43*(16), 8654–8661. https://doi.org/10.1002/2016GL069462

Chang, M.-H., Tang, T. Y., Ho, C.-R., & Chao, S.-Y. (2013). Kuroshio-induced wake in the lee of Green Island off Taiwan. *Journal of Geophysical Research: Oceans*, *118*(3), 1508–1519. https://doi.org/10.1002/jgrc.20151

Chang, Y.-L., & Oey, L.-Y. (2011). Interannual and seasonal variations of Kuroshio transport east of Taiwan inferred from 29 years of tide-gauge data. *Geophysical Research Letters*, *38*, L08603. https://doi.org/10.1029/2011gl047062

Chao, S.-Y., Ko, D.-S., Lien, R.-C., & Shaw, P.-T. (2007). Assessing the west ridge of Luzon Strait as an internal wave mediator. *Journal of Oceanography*, *63*(6), 897–911. https://doi.org/10.1007/s10872-007-0076-8

Chen, Y.-J., Shan Ko, D., & Shaw, P.-T. (2013). The generation and propagation of internal solitary waves in the South China Sea. *Journal of Geophysical Research: Oceans*, *118*, 6578–6589. https://doi.org/10.1002/2013JC009319

Cheng, Y.-H., Ho, C.-R., Zheng, Q., Qiu, B., Hu, J., & Kuo, N.-J. (2017). Statistical features of eddies approaching the Kuroshio east of Taiwan Island and Luzon Island. *Journal of Oceanography*, *73*(4), 427–438. https://doi.org/10.1007/s10872-017-0411-7

Davies, P. A., Besley, P., & Boyer, D. L. (1989). An experimental study of flow past a triangular cape in a linearly stratified fluid. *Dynamics of Atmospheres and Oceans*, *14*, 497–528. https://doi.org/10.1016/0377-0265(89)90076-6

Deem, G. S., & Zabusky, N. J. (1978). Vortex waves: Stationary "V states," interactions, recurrence, and breaking. *Physical Review Letters*, *40*(13), 859–862. https://doi.org/10.1103/PhysRevLett.40.859

Dong, C., McWilliams, J. C., & Shchepetkin, A. F. (2007). Island wakes in deep water. *Journal of Physical Oceanography*, *37*(4), 962–981. https://doi.org/10.1175/JPO3047.1

Farmer, D., Pawlowicz, R., & Jiang, R. (2002). Tilting separation flows: A mechanism for intense vertical mixing in the coastal ocean. *Dynamics of Atmospheres and Oceans*, *36*(1), 43–58. https://doi.org/10.1016/S0377-0265(02)00024-6

Fassbender, A. J., Bourbonnais, A., Clayton, S., Gaube, P., Omand, M., Franks, P. J. S., et al. (2018). Interpreting mosaics of ocean biogeochemistry. *Eos*, *99*. https://doi.org/10.1029/2018EO109707

Gula, J., Molemaker, M. J., & McWilliams, J. C. (2014). Submesoscale cold filaments in the Gulf Stream. *Journal of Physical Oceanography*, *44*(10), 2617–2643. https://doi.org/10.1175/JPO-D-14-0029.1

Gula, J., Molemaker, M. J., & McWilliams, J. C. (2015). Topographic vorticity generation, submesoscale instability and vortex street formation in the Gulf Stream. *Geophysical Research Letters*, *42*, 4054–4062. https://doi.org/10.1002/2015gl063731

Hasegawa, D., Yamazaki, H., Lueck, R. G., & Seuront, L. (2004). How islands stir and fertilize the upper ocean. *Geophysical Research Letters*, *31*, L16303. https://doi.org/10.1029/2004gl020143

Hsin, Y.-C., Qiu, B., Chiang, T.-L., & Wu, C.-R. (2013). Seasonal to interannual variations in the intensity and central position of the surface Kuroshio east of Taiwan. *Journal of Geophysical Research: Oceans*, *118*, 4305–4316. https://doi.org/10.1002/jgrc.20323

Jan, S., & Chen, C.-T. A. (2009). Potential biogeochemical effects from vigorous internal tides generated in Luzon Strait: A case study at the southernmost coast of Taiwan. *Journal of Geophysical Research*, *114*, C04021. https://doi.org/10.1029/2008JC004887

Jan, S., Mensah, V., Andres, M., Chang, M.-H., & Yang, Y. J. (2017). Eddy-Kuroshio interactions: Local and remote effects. *Journal of Geophysical Research: Oceans*, *122*, 9744–9764. https://doi.org/10.1002/2017JC013476

Jan, S., Yang, Y. J., Wang, J., Mensah, V., Kuo, T.-H., Chiou, M.-D., et al. (2015). Large variability of the Kuroshio at 23.75°N east of Taiwan. *Journal of Geophysical Research: Oceans*, *120*, 1825–1840. https://doi.org/10.1002/2014JC010614

Johns, W. E., Lee, T. N., Zhang, D., Zantopp, R., Liu, C.-T., & Yang, Y. (2001). The Kuroshio east of Taiwan: Moored transport observations from the WOCE PCM-1 array. *Journal of Physical Oceanography*, *31*(4), 1031–1053. https://doi.org/10.1175/1520-0485(2001)031<1031:Tkeotm>2.0.Co;2

Johnston, T. S., MacKinnon, J. A., Colin, P. L., Haley, P. J. Jr., Lermusiaux, P. F., Lucas, A. J., et al. (2019). Energy and momentum lost to wake eddies and lee waves generated by the north equatorial current and tidal flows at Peleliu, Palau. *Oceanography*, *32*(4), 110. https://doi.org/10.5670/oceanog.2019.417

Kang, D., & Curchitser, E. N. (2015). Energetics of eddy–mean flow interactions in the Gulf Stream region. *Journal of Physical Oceanography*, *45*(4), 1103–1120. https://doi.org/10.1175/JPO-D-14-0200.1

Ko, D. S., Chao, S.-Y., Huang, P., & Lin, S. F. (2009). Anomalous upwelling in nan wan: July 2008. *Terrestrial, Atmospheric and Oceanic Sciences*. https://doi.org/10.3319/TAO.2008.11.25.01(Oc

Kuehl, J. J., & Sheremet, V. A. (2009). Identification of a cusp catastrophe in a gap-leaping western boundary current. *Journal of Marine Research*, *67*(1), 25–42. https://doi.org/10.1357/002224009788597908

Lee, H.-J., Chao, S.-Y., Fan, K.-L., Wang, Y.-H., & Liang, N.-K. (1997). Tidally induced upwelling in a semi-enclosed basin: Nan Wan Bay. *Journal of Oceanography*, *53*, 467–480.

Lee, I.-H., Ko, D. S., Wang, Y.-H., Centurioni, L., & Wang, D.-P. (2013). The mesoscale eddies and Kuroshio transport in the western North Pacific east of Taiwan from 8-year (2003-2010) model reanalysis. *Ocean Dynamics*, *63*(9-10), 1027–1040. https://doi.org/10.1007/s10236-013-0643-z

Lévy, M., Ferrari, R., Franks, P. J. S., Martin, A. P., & Rivière, P. (2012). Bringing physics to life at the submesoscale. *Geophysical Research Letters*, *39*, L14602. https://doi.org/10.1029/2012GL052756

Leweke, T., Dizès, S. L., & Williamson, C. H. K. (2016). Dynamics and instabilities of vortex pairs. *Annual Review of Fluid Mechanics*, *48*(1), 507–541. https://doi.org/10.1146/annurev-fluid-122414-034558

Liang, W. D., Tang, T. Y., Yang, Y. J., Ko, M. T., & Chuang, W. S. (2003). Upper-ocean currents around Taiwan. *Deep Sea Research Part II: Topical Studies in Oceanography*, *50*(6), 1085–1105. https://doi.org/10.1016/S0967-0645(03)00011-0

Lien, R.-C., Ma, B., Cheng, Y.-H., Ho, C.-R., Qiu, B., Lee, C. M., & Chang, M.-H. (2014). Modulation of Kuroshio transport by mesoscale eddies at the Luzon Strait entrance. *Journal of Geophysical Research: Oceans*, *119*, 2129–2142. https://doi.org/10.1002/2013JC009548

Liu, C.-L., & Chang, M.-H. (2018). Numerical studies of submesoscale island wakes in the Kuroshio. *Journal of Geophysical Research: Oceans*, *123*, 5669–5687. https://doi.org/10.1029/2017JC013501

Liu, K.-K., Kang, C.-K., Kobari, T., Liu, H., Rabouille, C., & Fennel, K. (2014). Biogeochemistry and ecosystems of continental margins in the western North Pacific Ocean and their interactions and responses to external forcing—An overview and synthesis. *Biogeosciences*, *11*, 7061–7075. https://doi.org/10.5194/bg-11-7061-2014

Lumpkin, R., Özgökmen, T., & Centurioni, L. (2017). Advances in the application of surface drifters. *Annual Review of Marine Science*, *9*(1), 59–81. https://doi.org/10.1146/annurev-marine-010816-060641

Ma, B. B., Lien, R.-C., & Ko, D. S. (2013). The variability of internal tides in the Northern South China Sea. *Journal of Oceanography*, *69*(5), 619–630. https://doi.org/10.1007/s10872-013-0198-0

MacKinnon, J. A., Alford, M. H., Voet, G., Zeiden, K. L., Shaun Johnston, T. M., Siegelman, M., et al. (2019). Eddy wake generation from broadband currents near Palau. *Journal of Geophysical Research: Oceans*, *124*, 4891–4903. https://doi.org/10.1029/2019JC014945

Molemaker, M. J., McWilliams, J. C., & Dewar, W. K. (2015). Submesoscale instability and generation of mesoscale anticyclones near a separation of the. *California Undercurrent*, *45*(3), 613–629. https://doi.org/10.1175/JPO-D-13-0225.1

Nagai, T., Hasegawa, D., Tanaka, T., Nakamura, H., Tsutsumi, E., Inoue, R., & Yamashiro, T. (2017). First evidence of coherent bands of strong turbulent layers associated with high-wavenumber internal-wave shear in the upstream Kuroshio. *Scientific Reports*, *7*(1), 14,555. https://doi.org/10.1038/s41598-017-15167-1

Nitani, H. (1972). Beginning of the Kuroshio. In H. Stommel, & K. Yoshida (Eds.), *Kuroshio: Its physical aspects*, (pp. 129–163). Tokyo: University of Tokyo.

Oppenheim, A. V. (2010). *Discrete-time signal processing*, (3rd ed.). Upper Saddle River, NJ: Prentice Hall.

Pickering, A., Alford, M., Nash, J., Rainville, L., Buijsman, M., Ko, D. S., & Lim, B. (2015). Structure and variability of internal tides in Luzon Strait. *Journal of Physical Oceanography*, *45*(6), 1574–1594. https://doi.org/10.1175/jpo-d-14-0250.1

Pun, I.-F., Chan, J. C. L., Lin, I.-I., Chan, K. T. F., Price, J. F., Ko, D. S., et al. (2019). Rapid intensification of Typhoon Hato (2017) over shallow water. *Sustainability*, *11*(13), 3709. https://doi.org/10.3390/su11133709

Qian, H., Shaw, P.-T., & Ko, D. S. (2010). Generation of internal waves by barotropic tidal flow over a steep ridge. *Deep Sea Research Part I*, *57*(12), 1521–1531. https://doi.org/10.1016/j.dsr.2010.09.001

Rogers, J. S., Rayson, M. D., Ko, D. S., Winters, K. B., & Fringer, O. B. (2019). A framework for seamless one-way nesting of internal wave-resolving ocean models. *Ocean Modelling*, *143*, 101,462. https://doi.org/10.1016/j.ocemod.2019.101462

Saffman, P. G., & Szeto, R. (1980). Equilibrium shapes of a pair of equal uniform vortices. *The Physics of Fluids*, *23*(12), 2339–2342. https://doi.org/10.1063/1.862935

Savtchenko, A., Ouzounov, D., Ahmad, S., Acker, J., Leptoukh, G., Koziana, J., & Nickless, D. (2004). Terra and Aqua MODIS products available from NASA GES DAAC. *Advances in Space Research*, *34*(4), 710–714. https://doi.org/10.1016/j.asr.2004.03.012

Simmons, H., Chang, M.-H., Chang, Y.-T., Chao, S.-Y., Fringer, O., Jackson, C. R., & Ko, D. S. (2011). Modeling and prediction of internal waves in the South China Sea. *Oceanography*, *24*(4), 88–99. https://doi.org/10.5670/oceanog.2011.97

Smyth, W. D., and Carpenter, J. R. (2019). Instabilities of a parallel shear flow. In *Instability in Geophysical Flows*, (pp. 31–60). Cambridge University Press, Cambridge.

Sun, R., Gu, Y., Li, P., Li, L., Zhai, F., & Gao, G. (2016). Statistical characteristics and formation mechanism of the Lanyu cold eddy. *Journal of Oceanography*, *72*(4), 641–649. https://doi.org/10.1007/s10872-016-0361-5

Thomas, L., & Ferrari, R. (2008). Friction, frontogenesis, and the stratification of the surface mixed layer. *Journal of Physical Oceanography*, *38*(11), 2501–2518. https://doi.org/10.1175/2008jpo3797.1

Tseng, R.-S., Shao, H.-J., Chang, Y.-C., & Centurioni, L. (2012). Turbulent mixing of the Kuroshio waters Southeast of Taiwan. *Kuroshio Science*, *6-1*, 27–34.

Tsutsumi, E., Matsuno, T., Lien, R.-C., Nakamura, H., Senjyu, T., & Guo, X. (2017). Turbulent mixing within the Kuroshio in the Tokara Strait. *Journal of Geophysical Research: Oceans*, *122*, 7082–7094. https://doi.org/10.1002/2017JC013049

Warn-Varnas, A., Ko, D. S., & Gangopadhyay, A. (2015). Signatures of tidal interference patterns in the South China Sea. *Journal of Oceanography*, *71*(3), 251–262. https://doi.org/10.1007/s10872-015-0282-8

Williamson, C. H. K. (1996). Vortex dynamics in the cylinder wake. *Annual Review of Fluid Mechanics*, *28*(1), 477–539. https://doi.org/10.1146/annurev.fl.28.010196.002401

White, B., & Helfrich, K. (2013). Rapid gravitational adjustment of horizontal shear flows. *Journal of Fluid Mechanics*, *721*, 86–117.

Zeiden, K. L., Rudnick, D. L., & MacKinnon, J. A. (2019). Glider observations of a mesoscale oceanic island wake. *Journal of Physical Oceanography*, *49*(9), 2217–2235. https://doi.org/10.1175/jpo-d-18-0233.1

Zhang, D., Lee, T. N., Johns, W. E., Liu, C.-T., & Zantopp, R. (2001). The Kuroshio east of Taiwan: Modes of variability and relationship to interior ocean mesoscale eddies. *Journal of Physical Oceanography*, *31*(4), 1054–1074. https://doi.org/10.1175/1520-0485(2001)031<1054:Tkeotm>2.0.Co;2

Zheng, Q., Lin, H., Meng, J., Hu, X., Song, Y. T., Zhang, Y., & Li, C. (2008). Sub-mesoscale ocean vortex trains in the Luzon Strait. *Journal of Geophysical Research*, *113*(C4). https://doi.org/10.1029/2007JC004362